Post-Print of an Accepted Manuscript on the Laboratory of Turbulent Flows Website

Complete citation:

Ahmadi, F., Sanders, S., & Ghaemi, S. (2020). Experimental investigation of three-dimensional flow around particles in a turbulent channel flow. *Physical Review Fluids*, *5*(1), 014302. doi: 10.1103/PhysRevFluids.5.014302

The final publication is available at https://doi.org/10.1103/PhysRevFluids.5.014302

The Accepted Manuscript begins on the next page.

Experimental investigation of three-dimensional flow around particles in a turbulent channel flow

Farzad Ahmadi[1], Sean Sanders[2], and Sina Ghaemi[1*]

[1] Department of Mechanical Engineering, University of Alberta, Edmonton, Alberta, Canada, T6G 2G8

[2] Department of Chemical and Material Engineering, University of Alberta, Edmonton, Alberta, Canada, T6G 2V4

Abstract

The interaction between particles and turbulent flow is investigated by simultaneous measurement of the time-resolved three-dimensional (3D) velocity of particles and the carrier liquid phase. The investigation is conducted in a horizontal channel flow at a Reynolds number, *Re*, of 20,000, based on the average velocity and full channel height. The particle-laden suspension is produced by nearly neutrally buoyant beads with a density of 1.05 g/cm^3 and a mean diameter of 370 μm at a volumetric concentration of 0.1%. The liquid phase is seeded with 2 μm tracers, the images of which are digitally separated from the larger beads using a medina filter, and processed using time-resolved 3D particle tracking velocimetry. Conditional sampling of the beads and their surrounding fluid, based on the beads' wall-normal motion, showed that ascending beads were mostly located within ejection motions of the fluid. However, the descending beads did not indicate any correlation with the streamwise fluid velocity; the beads were surrounded by wall-ward fluid motions with both positive and negative streamwise velocity fluctuations. For both ascending and descending beads, the surrounding fluid motion had a strong spanwise velocity component. Inspection of the 3D beads' pathlines showed a spiral motion of beads around a streamwise axis. At $y/h < 0.2$, the descending beads showed a stronger correlation with their surrounding fluid, while ascending beads demonstrated a stronger correlation with their surrounding flow farther away from the wall. Conditional sampling of the beads and their surrounding flow was also performed based on the streamwise acceleration of the beads. The results showed that, in the near-wall region of $y/h < 0.2$, slip velocity and the resultant drag force were not in the same direction as the bead acceleration. Therefore, for this near-wall region, the drag force is not sufficient to model the dynamics of the large nearly buoyant beads.

Keywords: Particle-laden flow, Fluid-particle interaction, Particle tracking velocimetry

[*] Corresponding author
E-mail address: ghaemi@ualberta.ca (S. Ghaemi).

1. Introduction

The transport of solid particles by turbulent liquid flows occurs abundantly in nature and in industry; two disparate examples are particle transport in river flows and mining pipelines. In these particle-laden flows, the mutual forces between the particles and the liquid are critical to particle deposition and suspension, and erosive wear of the conduit. Therefore, to understand and model these systems, investigation is required ~~of~~ for the motion of both the solid phase and the surrounding liquid phase.

In turbulent wall flows, suspended particles that are heavier than the liquid phase move successively towards and away from the bottom wall (Sutherland 1967; Sumer 1974). Sumer and Oguz (1978) applied a photographic technique and recorded the trajectory of inertial particles over a smooth surface. They concluded that the ejection motions of the liquid phase transport the particles away from the wall and generate a negative streamwise velocity fluctuation (Sumer and Oguz 1978; Rashidi et al. 1990; Ji et al. 2013). Once the ejection motion attenuates, the suspended particles gradually approach the wall and may be lifted up again by another ejection motion, keeping the inertial particles suspended. For inertial particles that are smaller than the viscous sublayer thickness, Yung et al. (1989) observed that the particles initially slide on the wall and then are lifted up by ejection motions.

The interaction of particles with the liquid phase has traditionally been investigated based on whether the particles ascend from, or descend to, the bottom wall. The ascending particles typically originate from the slower near-wall flow, and therefore have a lower mean streamwise velocity than the descending particles (Nino and Garcia 1996). To scrutinize the relation between the particles' motion and the surrounding fluid, Kiger and Pan (2002) performed a simultaneous planar particle image velocimetry (PIV) of inertial particles and their surrounding liquid flow. They confirmed a preferential accumulation of ascending particles in the ejection motions, while less accumulation of descending particles was observed in the sweep motions of the liquid phase. Lelouvetel et al. (2009) showed that the quadrant distribution of liquid velocity fluctuations around the descending particles was similar to that of the unladen flow, suggesting a lack of correlation between the descending beads and the liquid phase turbulence. In contrast, more than half of the ascending particles were located in the ejection motions of the liquid phase, which showed a stronger correlation between ascending particles and the surrounding fluid. A poorer correlation of descending beads with sweep motions was also observed by van Hout (2011) in a square channel flow for nearly neutrally buoyant particles.

A few investigations have shown that suspension of particles is not only accompanied by ascending and descending motions. The DNS of Brooke et al. (1992) observed that inertial particles also have a strong spanwise velocity. In an experimental study of polystyrene beads, Kaftori et al. (1995) associated the ascending and descending motion of the beads to streamwise vorticity. Using DNS, Marchioli and Soldati (2002) observed that sweep and ejection motions are generated by the downwash and upwash sides of quasi-streamwise vortices. Their DNS was

carried out for particles smaller than the inner length-scale, and with a Stokes number, *St*, of 30. Here, *St* was calculated as the ratio of the particle response time to the inner time-scale of the turbulent flow. The volumetric concentration of particles was also 6.0×10^{-3}%, which indicates a one-way coupling where the particles have a negligible effect on the flow statistics (Elghobashi 1991). However, the role of the spanwise motions and quasi-streamwise vortices in transport of larger particles and at higher volumetric concentrations still has to be evaluated.

The investigation of the turbulent fluid flow surrounding finite-size particles has been limited by challenges in both numerical simulations and experimental techniques. A large number of numerical simulations have applied the classical point-particle method for modeling particles that are smaller than the smallest turbulent eddies present in the flow (e.g. Zhao et al. 2013; Lee & Lee 2019). These investigations have resulted in significant progress for understanding the behavior of sub-Kolmogorov particles (e.g. Soldati & Marchiolo 2009; Sardina et al. 2012). However, such a method may not be applicable to finite-size particles since it only considers the drag force, while forces such as lift, added-mass, and basset history forces are neglected. For an accurate simulation of flow surrounding finite-size particles, advanced interface-resolved simulations are required (e.g. Lashgari et al. 2016; Costa et al. 2018). Further, measurement of the liquid phase surrounding finite-size particles is also experimentally challenging because of blockage effects and strong reflections of the laser light by the large particles. The few available experiments have also been limited to a wall-normal-streamwise plane, which does not provide access to the spanwise motion of the particles and the surrounding fluid.

In the current investigation, we extend the previous analysis to higher particle concentration, investigate the 3D motion of the surrounding flow, and use the acceleration of particles to elucidate the momentum exchange of the particles with the surrounding fluid. We suggest that a particle sampling approach using particle acceleration can be more effective since it indicates momentum exchange between the particles and the surrounding flow. We have carried out simultaneous 3D measurement of particles and their surrounding fluid velocity in a suspension of nearly neutrally buoyant beads in a horizontal turbulent channel flow of water at a Reynolds number, *Re*, of 20,000. Large particles with a normalized diameter, d_p^+, of 26 and *St* of 2.7 are used. Here, d_p^+ is normalized by the wall unit. The volume concentration is 0.1%, in which two-way coupling between particles and fluid is expected. Time-resolved volumetric particle tracking velocimetry (PTV) based on the shake-the-box (STB) algorithm (Schanz et al. 2016) is performed. This PTV method makes it possible to perform measurements at high particle volumetric concentrations of 0.1%, in comparison with the previous 3D-PTV measurements in particle-laden flows, such as Suzuki et al. (2000) at 0.03%, and Oliveira et al. (2013, 2015) at 1.4×10^{-3}%. Based on their wall-normal motion and acceleration, the obtained Lagrangian particle tracks are used to conditionally sample the surrounding fluid. The 3D trajectories of the beads are also inspected for their 3D motion.

2. Experimental setup and measurements

2.1. Slurry flow loop

The experiments were carried out in a horizontal flow loop, as shown in Fig. 1. A centrifugal pump (LCC-M, GIW Industries Inc.) and a variable frequency drive (A510, Teco Electric & Machinery Co., Ltd.) were used to circulate the flow at a constant flow rate of 2.08 kg/s during the experiments. The mass flow rate was measured by a Coriolis flow meter (Micro Motion, F-Series) with an accuracy of ±0.10% of the measured rate. Measurements were conducted in a test section with rectangular cross-section, which had a full height of h = 15 mm in the wall-normal direction (y), and a width of 120 mm in the spanwise direction (z). The channel sidewalls were made of cast acrylic, while the top plate was made of glass for better light transmission and reduced image distortion. The total length of the channel was 2.5 m (166h) in the streamwise direction (x). To ensure a fully developed turbulent flow, the measurement domain was 1.65 m (110h) downstream of the channel entrance. The bulk Re was 20,000, based on the full channel height and the average velocity, U_{avg} of 1.16 m/s. The friction Reynolds number, Re_τ, was equal to 1090, defined as $u_\tau h/\nu$, where u_τ and ν are friction velocity and kinematic viscosity, respectively. The flow loop also utilized a double-pipe heat exchanger to maintain the fluid temperature at 25±0.1°C. Two data acquisition cards (NI 9211, 9263, National Instrument) were used to record the mass flow rate, fluid temperature and density (ρ_f) at a sampling rate of 1 Hz, and to control the variable frequency drive.

For the particulate phase, polystyrene spherical beads with a density (ρ_b) of 1.05 g/cm^3, and at a volumetric concentration (φ_v) of 0.1%, were used. The mean diameter of beads (d_b) was 370 μm with a standard deviation of 35 μm. The size distribution of the beads was obtained from 30,000 images with a digital resolution of 69 pix/mm. The images were processed using the 'imfindcircle' function (MATLAB R2015b, The MathWork Inc.), which uses Circle Hough Transform (CHT) (Atherton and Kerbyson 1999) to find the diameter of the beads. About 61% of the data were within one standard deviation of the mean.

The liquid flow was also seeded with 2 μm silver-coated glass beads (SG02S40 Potters Industries) at a concentration of 8×10^{-3} (% by volume) to obtain the velocity of the fluid phase. These tracers have a density of 4 gr/cm^3 and are seven times smaller than the wall unit. Their response time is 1.0 μs with St of 3.2×10^{-3}. The latter was calculated using the inner time scale of the turbulent flow, as will be discussed in the following paragraphs.

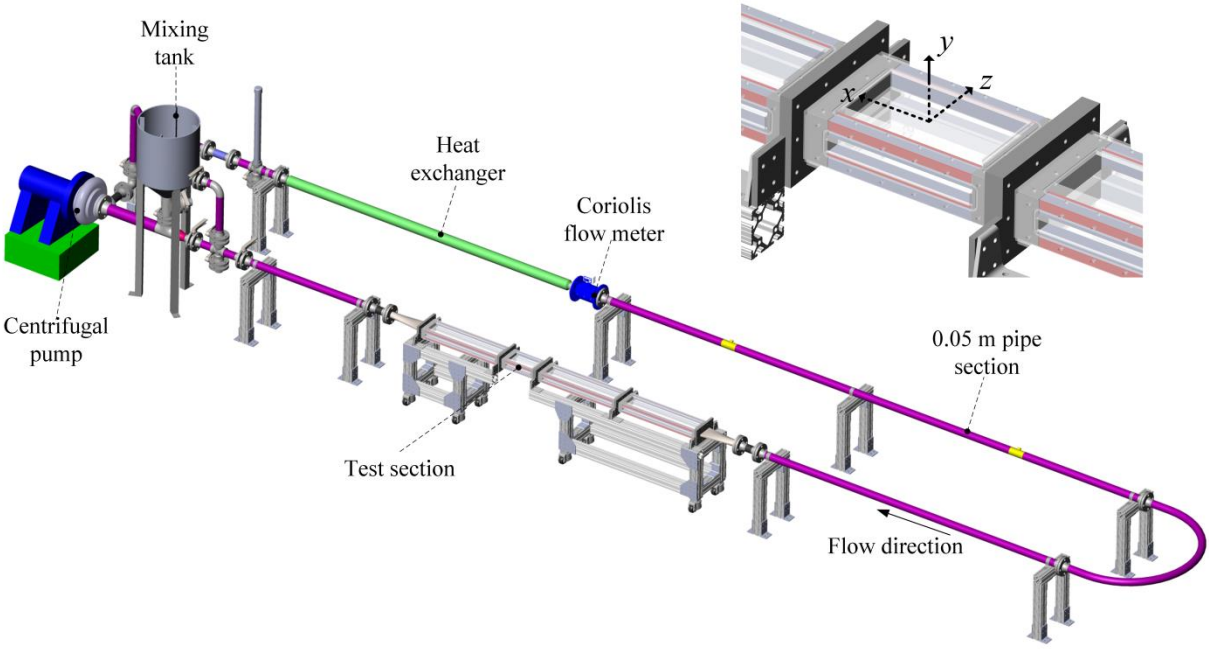

Fig. 1. Schematic of the flow loop demonstrating its main components. The inset shows the test section and the streamwise (x), wall-normal (y), and the spanwise (z) directions. The origin of the coordinate system is on the bottom wall of the channel.

The analysis of the velocity field is carried out using dimensionless parameters, which are normalized by outer and inner scales of the turbulent channel flow. The average velocity of unladen flow across the channel height (U_{avg}) and the channel height (h) are used as the outer velocity and length scales, respectively. Inner scaling includes the friction velocity, u_τ, and the inner length scale (λ) of the unladen flow, which are equal to 0.062 m/s and 14.05 μm, respectively. The inner scaling is obtained using the Clauser method (Clauser 1956), and the parameters normalized using inner scaling are indicated by a superscript '$^+$'. The turbulent scales are estimated from the 4D-PTV measurements of the mean velocity profile, as detailed in Section 2.2. The inner length scale of the flow results in $d_b^+ = d_b/\lambda = 26$.

The response of the beads to fluid motion is characterized using the Stokes number (St), which is the ratio of the beads' response time to a characteristic time scale of the flow. The latter parameter can be estimated using the viscous time scale $\tau_v = \upsilon/u_\tau^2$, where υ is the kinematic viscosity of the fluid. The bead response time, τ_b, is also calculated as (van Hout 2013)

$$\tau_b = \frac{(\rho_b - \rho_f) d_b^2}{18\mu}, \qquad (1)$$

where μ is the fluid dynamic viscosity. In this equation, the settling velocity of a bead is normalized by the gravitational acceleration. This equation was used by van Hout (2013) and Bellani et al. (2012). The estimated time scales are τ_v = 0.23 ms and τ_b = 0.62 ms, which result in a bead St of 2.7. This estimation of St applies to the inner layer, since the flow time scale increases with distance

from the wall. The local *St* is expected to reach its minimum value at the centre of the channel. Another approach for estimation of τ_b is to consider the response of the bead to a steady uniform flow based on $\tau_b = \rho_b d_b^2/18\mu$. This equation results in a larger τ_b, and *St* of 54. The settling parameter, $v_s/\kappa u_\tau$, is about 0.2, showing that the effect of gravity is small. In this parameter, v_s is the terminal settling velocity of the beads and κ is the von Kármán constant (Sumer and Oguz 1978; Marchioli et al. 2008). The estimated Shields number, $(\rho_f u_\tau^2)/([\rho_b-\rho_f]d_p)$, is about 15, which also indicates small gravitational effects with respect to wall shear stress (Miller et al. 1977). For the current volumetric concentration of 0.1%, the ratio of the mean distance between the beads (*S*) to bead diameter (d_b), S/d_b, is 12. According to the criterion suggested by Elghobashi (1991), a small probability of particle-particle collision exists at $\varphi_v = 0.1\%$, and $S/d_b \sim 12$. The two-phase flow at this concentration is also classified in the two-way coupling regime.

The investigations of van Hout (2011) and Shao et al. (2012) were carried out on particle-laden flows of solid-liquid in horizontal channels, and with similar particle-laden parameters with respect to the current experiments. Van Hout (2011) experimentally investigated the dynamics of nearly buoyant polystyrene beads with $d_b^+ = 12$ and $St = 0.27$. Shao et al. (2012) carried out a direct numerical simulation of beads with $\rho_b \sim 1.5\rho_f$, $d_b/h = 0.025$ (the same as the current experiment) and $d_b^+ = 10$. Both studies showed preferential distribution of beads in the low-speed region, suggesting its possibility for the current investigation.

2.2. Time-resolved three-dimensional PTV

A three-dimensional imaging system was used to simultaneously record time-resolved images of the particle-laden flow from four viewing angles. To distinguish the fluid tracers (2 μm) from the beads (370 μm), a median filter was applied to the images to increase their intensity contrast (Kiger and Pan 2000). Using a threshold intensity, the filtered images were decomposed to two sets: images of the tracers and images of the beads. To obtain 3D trajectories of the tracers and the beads, the two image sets were processed using a Lagrangian 3D particle tracking velocimetry based on the STB method (Schanz et al. 2016). This method enabled us to obtain simultaneous 3D measurement of both the solid and fluid phase velocity. Because of both the time-resolved and the 3D nature of these measurements, we refer to them here as 4D-PTV.

The measurement volume was illuminated using a dual-cavity Nd:YLF laser (Photonics Industries, dual-head DM-527 series) with a maximum energy of 20 mJ per pulse at a wavelength of 527 nm. The laser beam was expanded and collimated into a sheet 8 mm thick in the *y* direction and a width of 60 mm in the *x* direction. The laser sheet entered the channel along the *z* axis through the sidewall, as shown in Fig. 2. A mirror was located normal to the illumination direction (*z* axis) to reflect the light back into the test section to amplify the light intensity and to reduce the intensity difference between the forward and backward scattering cameras (Ghaemi and Scarano 2010). Knife-edge filters were attached to the sidewalls to remove the low-energy edges of the laser sheet and obtain a relatively top-hat intensity profile.

The imaging system consisted of four high-speed CMOS cameras (Phantom v611) with a sensor size of 1280×800 pix. Each pixel of the CMOS sensor is 20×20 μm^2 with 12-bit resolution. As shown in Fig. 2, the cameras imaged the measurement volume from the top of the test section through the glass window. The cameras were arranged in a plus-like configuration at a working distance of ~35 cm. The aperture angle, defined as the angle between two opposing cameras, was 65°. A camera lens with a focal length of f = 105 mm (Sigma) was connected to each camera using a lens-tilt adapter (Scheimpflug). The aperture size of each lens was set to f/22 to decrease any astigmatism effect on the particle images. The estimated depth-of-focus was 12 mm, which covered the thickness of the laser sheet. The magnification of each camera was 0.43 with a digital resolution of 22 pix/mm, which resulted in a measurement volume of 60×8×40 mm^3 in x, y and z directions, respectively. Using a high-speed controller (HSC v2, LaVision GmbH), the cameras were synchronized with the laser to acquire single-frame images at 6,000 Hz. Five sets of 5,500 time-resolved images were collected.

The initial calibration of the imaging system was performed using a dual-plane 3D calibration plate and the application of a third-order polynomial mapping function (Soloff et al. 1997). The root mean square (rms) of the fit error was less than 0.25 pix on both planes of the 3D target. The remaining calibration error was corrected using the volumetric self-calibration technique (Wieneke 2005, 2008). The volume self-calibration process was repeated several times to obtain a mean disparity of 0.026 pix with the standard deviation of 0.017 pix in the entire domain.

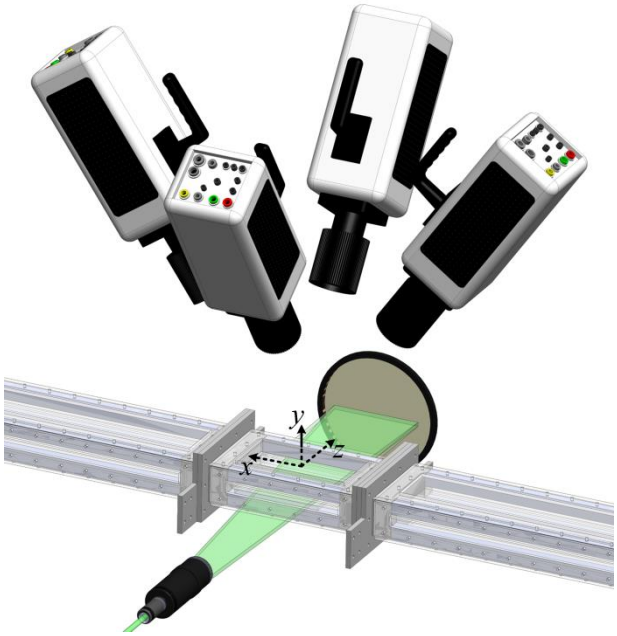

Fig. 2. Schematic of the four cameras and the laser sheet with respect to the channel and the coordinate system.

To reduce background noise, the minimum intensity of all the images was subtracted from each image, and the images were also normalized using the average intensity of the data set. The signal-to-noise ratio was further improved by subtracting a sliding minimum over a kernel of 30×30 pix

and local normalization by the average intensity in a kernel of 50×50 pix. To separate the beads from the tracers, a 6×6 pix median filter was applied. This filter reduced the intensity of the small tracers (~3 pix), but had a negligible effect on the intensity of the beads (~8 pix). An intensity threshold was then used to obtain a mask identifying the high intensity glass beads. The mask was applied to generate two sets of images for the beads and tracers based on the initial images (i.e., before applying the median filter). A Gaussian filter with a kernel of 7×7 pix was applied to the bead images to obtain a Gaussian intensity distribution. The volumetric concentration of beads resulted in an image number density of 0.005 particle per pixel (ppp), while the density of fluid phase tracers was 0.035 ppp. To evaluate the uncertainty of the measurement system and characterize the turbulent channel flow, unladen flow measurements were also carried out at a particle number density of 0.04 ppp. A summary of measurement parameters is provided in Table 1.

Table 1. Summary of the 4D-PTV system specifications.

Magnification	Digital resolution (pix/mm)	Acquisition frequency (kHz)	Field of view (mm^3)	Image diameter (pix)		Particle image density (ppp)	
				tracers	beads	tracers	beads
0.43	22	6	60×40×8	3	8	0.035	0.005

To obtain the optical transfer function (OTF) for the STB algorithm (Schanz et al. 2016), the measurement domain was divided into 15×8×9 sub-volumes in *x*, *y*, and *z* directions, respectively. In the OTF process, an elliptical Gaussian model is fitted to the particle shape for each sub-volume to include the distortion effects from astigmatism and blurring (Wieneke 2013). The fit area used for calculation of the OTF was 11×11 pix for the beads, and 3×3 pix for the tracers. The STB algorithm initiates particle tracking by detecting local intensity peaks. A maximum triangulation error of 1.0 and 0.5 pix was applied to the beads and the tracers, respectively. Particle pairs with spacing smaller than 2.0 pix were removed in the STB algorithm. For each image, the STB method performs an iterative triangulation process (also called outer loop) to detect particles that enter the domain. The position and intensity of all detected particles were updated through another iterative process (inner loop) that shakes the particles around the predicted position by 0.1 pix to find the optimal position (Schanz et al. 2016). Four outer loop iterations, followed by eight shaking iterations of the inner loop, were applied. The maximum displacement of particles between two successive frames was around 5 pix, and the allowable maximum particle shift was limited to 8.0 pix. Calculation of OTF and particle tracking was performed in Davis 8.4 (LaVision GmbH).

To increase particle positioning accuracy, a second-order polynomial was fitted to the time series of particle positions (particle tracks) through a weighted linear least squares ('rloess') function, MATLAB R2015b), as also applied by van Hout (2011) and Oliveira et al. (2013). A polynomial

kernel size of 40 time steps (equal to 6.6 ms) was applied to the beads and kernel of 20 time steps (3.3 ms) for the fluid phase. Using the relation given by Milojević (1990) and Schlichting and Gersten (2017) for a turbulent channel flow, the Kolmogorov time scale (τ_K) is 6.0 ms, which is greater than the 3.3 ms kernel size. This ensures that only measurement noise or turbulence fluctuations with negligible energy are filtered out. A larger kernel size was used for the beads since they have a longer response time than the fluid phase. The velocity and acceleration of the particles were also obtained from the coefficients of the second-order polynomial. The channel height is divided into 0.5 mm ($0.03h$) bins with 50% overlap to calculate the mean velocity and turbulence intensities. To obtain the fluid velocity surrounding a bead, the velocity of tracer particles is averaged in a cubic volume, where the bead is located at its centre. Different volume sizes were evaluated and it was found that the results are independent of the volume size when the volume is less than $1.4\times1.4\times1.4$ mm^3 ($3.8d_b\times3.8d_b\times3.8d_b$). This cubic volume around the bead is referred to as the 'surroundings' fluid.

The instantaneous velocity components are indicated by U, V, and W in streamwise, wall-normal, and spanwise directions, respectively. The instantaneous velocity is decomposed into mean, indicated by the symbol $\langle\ \rangle$, and velocity fluctuations shown by the lower case letters u, v, and w. The decomposition is expressed as $U = \langle U\rangle + u$. The average wall-normal and spanwise velocity is negligible in channel flow; hence, for these two components, instantaneous velocity is the same as velocity fluctuation, i.e. $V = v$ and $W = w$. Similar to Oliveira et al. (2015) and van Hout (2011), the velocity fluctuation of the beads is estimated as the difference between the instantaneous velocity of the bead and the average velocity of the liquid phase at the bead centroid, i.e. $u_b = U_b - \langle U_f\rangle$. The subscripts b and f refer to the bead and fluid phases, respectively.

3. Turbulent channel flow

In order to evaluate the uncertainty of the PTV system, the measurement in the unladen flow is compared with the DNS results of Lee and Moser (2015). The semi-logarithmic profile of mean velocity from 4D-PTV in the unladen flow at $Re_\tau = 1090$ ($Re = 20{,}000$), along with the DNS results of Lee and Moser (2015) at Re_τ of 1087, are shown in Fig. 3a. The measurements deviate from the law of the wall in the linear viscous sublayer ($y^+ < 5$), but the difference diminishes with increasing y^+. The discrepancy between 4D-PTV and DNS is smaller than 1.0% at $y^+ > 15$ ($y/h > 0.015$), which is equivalent to $0.1u_\tau$, or 0.02 pixel error in the estimation of particle displacement. The measurements agree with the logarithmic law, $\langle U_f\rangle^+ = 1/\kappa\ ln\ (y^+) + B$, where the von Kármán constant, κ, is equal to 0.38 and $B = 4.27$. This agreement confirms the accuracy of mean velocity at $y^+ > 5$ and the fully developed state of the turbulent channel flow. The large uncertainty at the near-wall region of $y^+ < 5$ is associated with the smaller displacement of the particles between the two laser pulses; maximum of 1 pix displacement. Another source of uncertainty in this region is due to the glare spots caused by the reflection of the laser from the surface. These reflections interfere with particle detection and also skew the calibration map during the self-calibration process. The mean disparity for the first calibration plane above the wall is 0.039 pix with standard

deviation of 0.019 pix. This is larger than 0.026 pix mean disparity and 0.017 pix standard deviation for the entire domain.

All four non-zero components of the Reynolds stress tensor for the unladen flow, obtained from 4D-PTV measurements, are shown in Fig. 3b and are also compared with the DNS results of Lee and Moser (2015). In general, the Reynolds stresses agree with the DNS. At y^+>15, the maximum absolute error relative to DNS is equivalent to 0.03, 0.02, and 0.02 pixels for $\langle {u_f}^2 \rangle$, $\langle {v_f}^2 \rangle$ and $\langle {w_f}^2 \rangle$, respectively. However, the smaller displacements in the y and z directions result in larger relative errors in $\langle {v_f}^2 \rangle$ and $\langle {w_f}^2 \rangle$. For example, the maximum discrepancy is 12.9% at $y^+ = 26$ for $\langle {v_f}^2 \rangle$. Overall, comparison of the 4D-PTV with the DNS results shows that measurements are accurate at $y^+ > 15$ ($y/h > 0.015$) with a maximum uncertainty of $0.1u_\tau$ (0.02 pixel) for the mean velocity and $0.15u_\tau$ (0.03 pixels) for the Reynolds stresses.

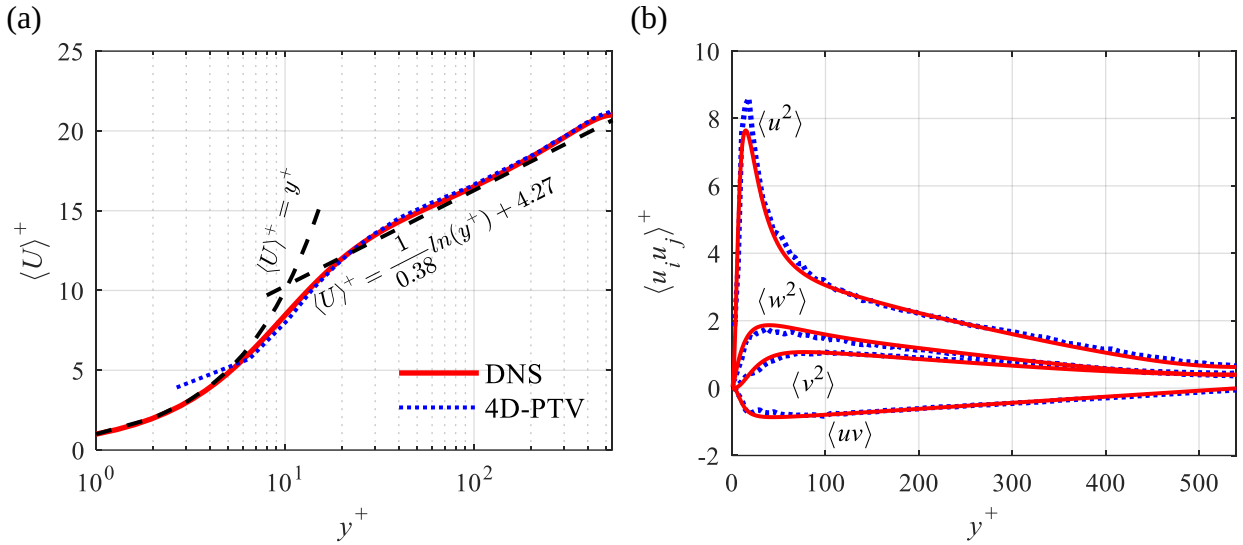

Fig. 3. Profiles of the normalized (a) mean streamwise velocity, and (b) Reynolds stresses for the unladen flow at Re_τ = 1090. The results are compared with the channel flow DNS results of Lee and Moser (2015) at Re_τ = 1087.

Figure 4 shows the mean velocity and Reynolds stresses of the beads and the suspending liquid phase from the simultaneous 4D-PTV measurements. In Fig. 4a, at $y^+ > 20$, the beads have a slightly lower mean velocity than the fluid. This suggests preferential accumulation of the beads in low-speed regions (Kiger and Pan 2002) as will be discussed in the next section. At smaller distances from the wall ($y^+ < 20$), the bead velocity is higher than the fluid velocity, which is associated with the rolling and sliding motions of the beads along the wall. These motions relax the no-slip boundary condition, i.e. the beads have a finite slip velocity at the channel wall. Figure 4b shows that the beads have larger Reynolds stresses than the fluid phase across the bottom half of the channel, although the difference is smaller for $\langle v^2 \rangle$ and $\langle uv \rangle$. The larger Reynolds stresses are associated with the relaxation time and St of the beads, which allows them to maintain their velocity for a longer time when transported in the wall-normal direction. As a result, the beads have a wider velocity distribution, which results in larger Reynolds stresses. Figure 4b also shows

that the difference between the intensities of the beads and the fluid phase decreases closer to the centre of the channel. In this region, the local *St* is smaller and the beads follow the fluctuations more closely.

In addition to the comparison with DNS results described earlier, an uncertainty analysis based on statistical convergence was conducted (see Appendix A) to estimate the random error. The estimated errors for the mean flow and Reynolds stresses are shown using error bars in Fig. 4 at selected wall-normal locations.

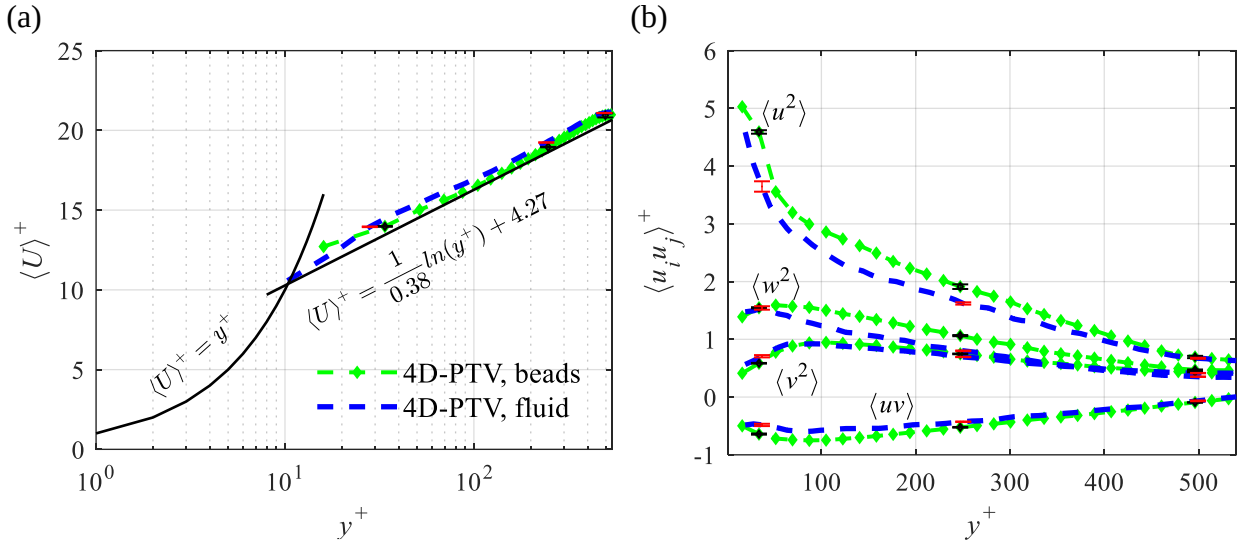

Fig. 4. Profiles of the normalized (a) mean streamwise velocity, and (b) Reynolds stresses for the beads and carrier fluid phase at Re_τ = 1090 and φ_v = 0.1% measured by 4D-PTV. The error bars show the estimated uncertainty based on Appendix A. Only three locations are chosen to show the error bars for clarity.

4. Ascending and descending beads

In this section, the velocity of the beads and their surrounding fluid is investigated by applying conditional sampling based on the wall-normal bead motion (ascending or descending). The reason for this sampling is to explore the fluid motions responsible for the upward and downward bead motions, which are subsequently important in the entrainment and deposition processes. The conditionally averaged parameters are indicated by subscript *c*. From a total of 1.7×10^7 detected bead images, 54% had a descending motion and the remaining 46% were ascending, away from the wall. The slightly greater number of descending beads is hypothesized to be related to the fact that the beads are slightly heavier than the fluid phase (ρ_b/ρ_f = 1.05).

4.1. Conditionally averaged velocity

The conditionally averaged streamwise velocity of the beads and their surrounding fluid, based on ascending ($V_b > 0$) and descending ($V_b < 0$) beads, is shown in Fig. 5a. The figure also shows the ensemble velocity of the fluid (without conditional sampling) as a baseline for comparison. The

ascending beads and the surrounding fluid have a lower velocity than the ensemble fluid velocity. This velocity lag was also observed by Kiger and Pan (2000) and van Hout (2011) and suggests preferential accumulation of the ascending beads in the low-speed regions. On the other hand, the descending beads and their surrounding fluid have approximately the same velocity as the ensemble fluid velocity. This agrees with Kiger and Pan's (2002) observation that the descending beads do not demonstrate any preferential clustering and are evenly distributed in high- and low-speed regions. The comparison of the beads and the fluid velocity in Fig. 5a also shows that the apparent slip velocity, defined as $\langle U_f \rangle_c$-$\langle U_b \rangle_c$, is positive and larger for the ascending beads. The maximum slip velocity of the ascending beads is about 8% of the ensemble fluid velocity and occurs at $y/h \sim 0.1$ ($y^+ \sim 100$), which is located in the outer layer.

The conditional averages of wall-normal and spanwise velocities, based on ascending and descending beads, are presented in Figs. 5b and 5c. The $\langle V_b \rangle_c$ profiles are symmetric for the ascending and descending beads with equal magnitudes but opposite sign. However, $\langle V_f \rangle_c$ is less than $\langle V_b \rangle_c$, which suggests a velocity lag or a reduced correlation between bead and fluid velocity in the wall-normal direction. Bead inertia (i.e. finite *St*) is expected to result in wall-normal velocities that persist longer than those of the surrounding flow, which contributes to the larger values $\langle V_b \rangle_c$.

Figure 5c presents the conditional average of the absolute value of the spanwise velocity, $\langle |W| \rangle_c$, for ascending and descending beads and their surrounding fluid. The absolute value is used to prevent zero averages caused by spanwise symmetry of the flow. For both ascending and descending beads, the spanwise velocity is higher than the wall-normal velocity. The $\langle |W| \rangle_c$ of both ascending and descending beads is higher than that of the surrounding fluid. The apparent spanwise slip velocity, $\langle |W_f| \rangle_c$-$\langle |W_b| \rangle_c$, is lower than the wall-normal counterpart, which suggests a higher correlation between spanwise motion of the beads and the fluid. The figure also shows that the ascending beads have a higher spanwise velocity than descending beads.

(a) (b) (c)

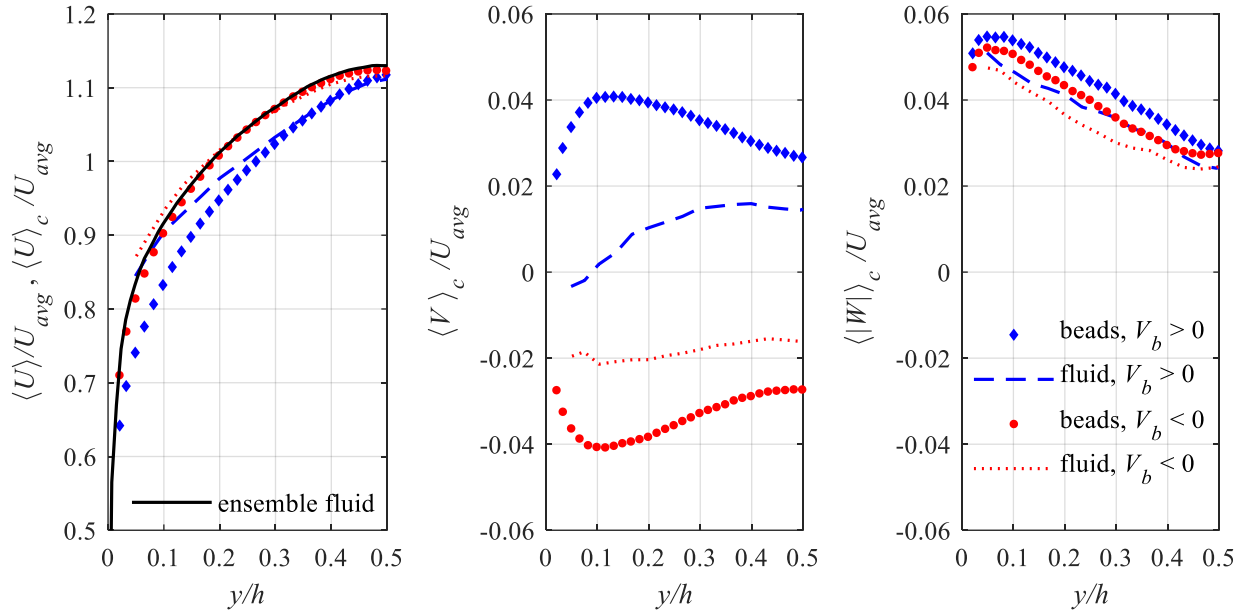

Fig. 5. Conditional average of (a) streamwise, (b) wall-normal, and (c) absolute spanwise velocity of the beads and their surrounding fluid based on the wall-normal direction of the beads.

4.2. Correlation of bead and surrounding fluid motions

To further investigate the fluid-particle interaction, the correlation of ascending and descending beads with the surrounding fluid is estimated here. The streamwise correlation is quantified using ρ_u, defined as

$$\rho_u = \frac{\langle u_b u_f \rangle}{\sqrt{\langle u_b{}^2 \rangle . \langle u_f{}^2 \rangle}}. \qquad (2)$$

Similar correlation coefficients are also defined for the wall-normal and spanwise directions using the corresponding velocity fluctuations, and indicated as ρ_v and ρ_w, respectively. Variation of the correlation coefficients for the ascending and descending beads across the bottom half of the channel is shown in Figs. 6a-c. With increasing distance from the bottom wall, the correlation coefficient of all the components increases. This occurs because the characteristic time scale of eddies increases with increasing distance from the wall (Tennekes and Lumley 1972), which reduces the local values of the bead *St*, making their motion correlate more strongly with the fluid fluctuations.

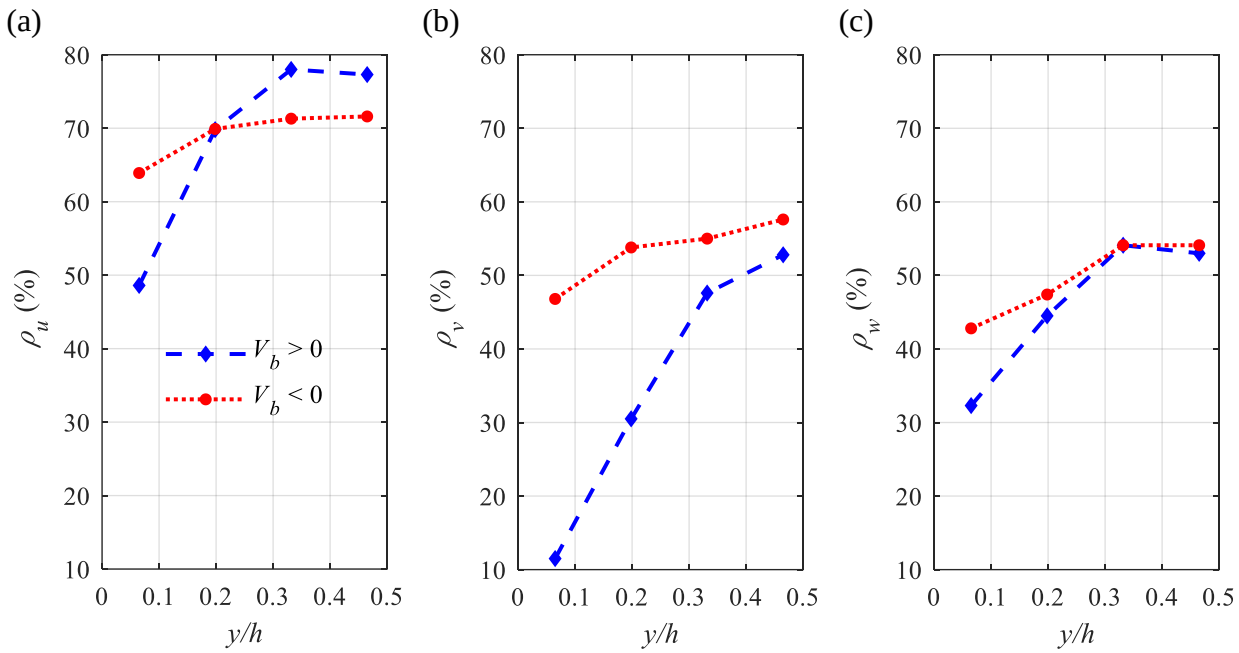

Fig. 6. The correlation coefficients of ascending and descending beads with their surrounding fluid in (a) streamwise, (b) wall-normal, and (c) spanwise directions.

For streamwise motions at $y/h < 0.2$ ($y^+ < 200$), the descending beads are more correlated with their nearby fluid than are the ascending beads. This trend reverses for $y/h > 0.2$, and a stronger correlation is observed for the ascending beads. The relationship is further investigated in Figs. 7a and 7b by quadrant analysis, in which the velocity fluctuations are considered in the four quadrants of a v versus u plot (Willmarth and Lu 1972). The quadrants of the plot are indicated by Q_1 ($u > 0$ and $v > 0$), Q_2 ($u < 0$ and $v > 0$), Q_3 ($u < 0$ and $v < 0$), and Q_4 ($u > 0$ and $v < 0$), and are referred to as outward interaction, ejection, inward interaction, and sweep, respectively. For each quadrant, the percentage of motion is calculated for the fluid surrounding the ascending and descending beads, and plotted in Fig. 7. In Fig. 7a, most of the ascending beads are surrounded by ejection fluid motions, and in Fig. 7b most of the descending beads are found within sweep events. At $y/h = 0.06$, 33% of ascending beads are situated in fluid ejections while 48% of descending beads reside in sweep motions. At $y/h < 0.2$ of Fig. 6a, this larger percentage of sweep motions by the descending beads results in their larger ρ_u with respect to the ascending beads. With increasing distance from the wall, the fraction of ejection motions around ascending beads increases, while a reduction in sweep events is observed for the descending beads, as shown in Fig. 7. This explains the larger values of ρ_u for ascending beads at $y/h > 0.2$ of Fig. 6a. Figure 6 also shows that ρ_u is stronger than ρ_v and ρ_w because of the greater momentum of streamwise fluid motions.

The correlation coefficient of the wall-normal velocity of ascending beads and their surrounding fluid is small in the immediate vicinity of the wall in Figure 6b. The small coefficient indicates that the beads do not follow the fluid ejection motions in the wall-normal direction. In Figure 6b,

descending beads are shown to have larger values of ρ_v than the ascending beads. Comparison of the results of Figs. 7a and 7b also shows that the total fraction of upward-moving fluid (i.e., the sum of fractions in Q_1 and Q_2) surrounding ascending beads is less than the fraction of downward flows (i.e., the sum of fractions in Q_3 and Q_4) around descending beads. This contributes to the larger ρ_v values of the descending beads. A similar trend is shown in Fig. 6c for correlations in the spanwise direction. Descending beads have a stronger correlation with the surrounding fluid relative to the ascending beads, although the difference in ρ_w for ascending and descending beads is smaller.

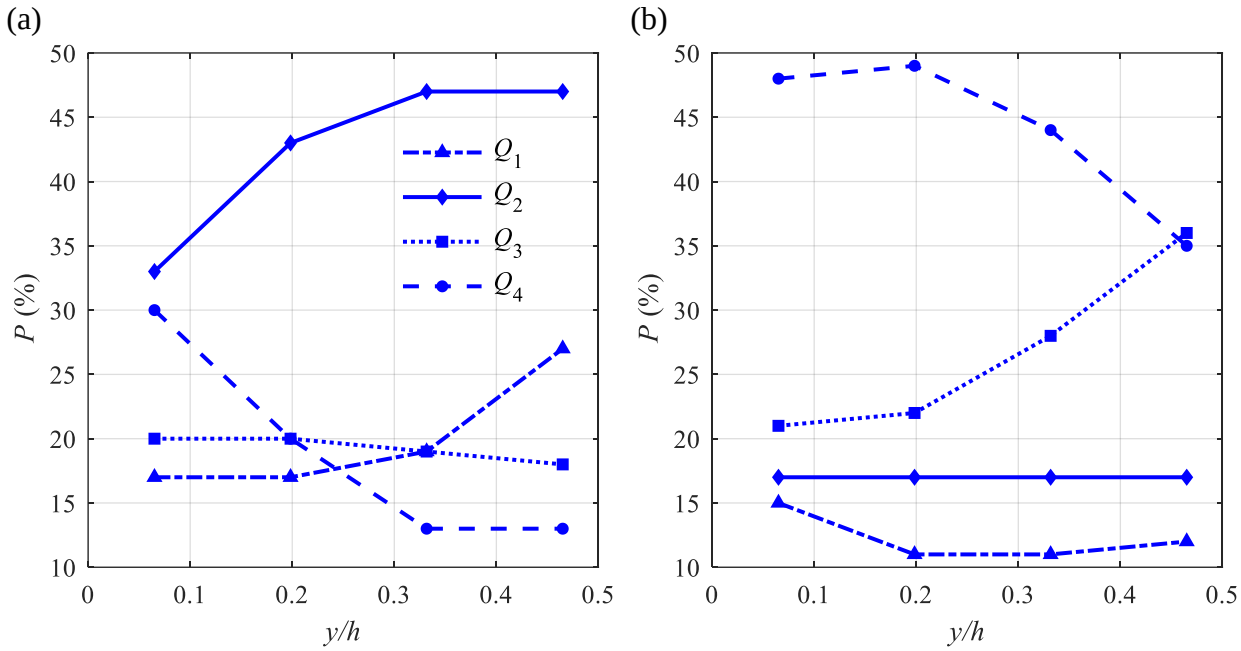

Fig. 7. The fraction of the fluid surrounding the (a) ascending and (b) descending beads based on the four quadrants of velocity fluctuations.

For a better interpretation of Fig. 6, the joint probability density function (JPDF) of velocity fluctuations for the ascending and descending beads is presented in Fig. 8 for the data within $0 < y/h < 0.26$. The JPDFs of u_b and u_f are shown in Fig. 8a, and the JPDF of the wall-normal (v_b, v_f) and spanwise (w_b, w_f) velocity fluctuations are shown in Figs. 8b and 8c, respectively. An assumed perfect correlation between the beads and the fluids would collapse the JPDF on the dashed lines shown in the figures (e.g., $u_b = u_f$), while a weak correlation would scatter the data around this line. In Fig. 8b, as expected, the JPDF of beads with negative and positive v_b only covers half of the figure. A slightly narrower JPDF is observed for the streamwise component of descending beads relative to the ascending beads in Fig. 8a; a stronger correlation of the descending beads with the surrounding fluid. In Fig. 8a, as expected, the JPDF of ascending beads skews negatively; for ascending beads, u_b and u_f are more likely to be negative. Figure 8c shows that ascending and descending beads have a similar JPDF distribution which agrees with the small difference between ρ_w of ascending and descending beads in Fig. 6c. This shows that there is no spanwise preference for the ascending and descending beads.

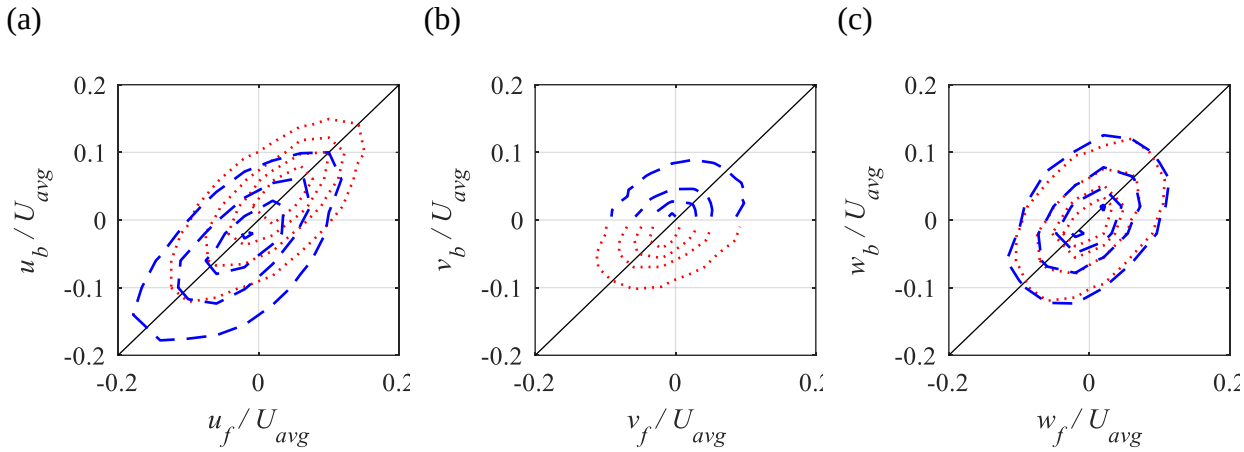

Fig. 8. JPDF of (a) streamwise (u_f, u_b), (b) wall-normal (v_f, v_b), and (c) spanwise (w_f, w_b) velocity of beads and surrounding fluid for $0 < y/h < 0.26$. The blue dashed contours show the results related to the ascending beads, and red dotted contours represent JPDF of descending beads. The JPDF percentages vary from 1.0% to 8.0% in steps of 2.3% for the most inner to the most outer contour, respectively.

The flow field around the particles was also studied by Lelouvetel et al. (2009) and van Hout (2011) using planar PIV. Lelouvetel et al. (2009) studied the accumulation of glass beads in ejection and sweep events in a free-surface channel flow without calculating any correlation coefficients. They stated that the ejection motions of the fluid significantly contribute to the ascending motion of the beads. However, there is no clear correlation between the turbulent events and the descending beads. Their statement does not agree with our results for descending beads presented in this section. This discrepancy can be attributed to the higher density of the glass beads compared with the nearly neutrally buoyant polystyrene beads used in this study. Because of gravity, the glass beads descend independent of the fluid motion, which weakens their correlation with the surrounding flow. In the other study, van Hout (2011) performed experiments in a one-way coupled flow ($\varphi_v = 0.014\%$) in a square channel at $Re = 15{,}000$. He observed that ascending polystyrene beads accumulate heavily in ejections at $y^+ > 50$, while descending beads show less accumulation in the sweeps. As presented in Figs. 7, more ascending beads accumulate in fluid ejections at $y/h > 0.25$ ($y^+ > 250$).

4.3. Velocity field around the beads

In this section, the 3D velocity fields around ascending and descending beads are investigated by obtaining the conditionally average fluid field in streamwise-wall-normal and streamwise-spanwise planes. For this purpose, similar to previous sections, the velocity of the surrounding fluid was sampled in a cubic volume of 1.4×1.4×1.4 mm^3 (0.09h×0.09h ×0.09h) with the bead located at its centre. The conditional samples of surrounding fluid were then averaged across the bottom half-channel $0 < y/h < 0.5$. The obtained conditional averages of fluid velocity fluctuations, $\langle u_f \rangle_c$ and $\langle v_f \rangle_c$, in the XY plane around ascending and descending beads are shown in Figs. 9a and 9b, respectively. In this figure, the streamwise and wall-normal relative locations of the tracers with respect to the bead are indicated as X and Y. The blank region at $Y < 0$ results from the bead

blocking the camera's line of sight. The blank region at $Y > 0$ is due to the overlap of the tracer images with the brighter bead image.

The conditional average of Fig. 9a shows that ascending beads are surrounded by an ejection motion of the fluid phase, in agreement with Kiger and Pan (2002) and Vinkovic et al. (2011). The streamwise component of fluid velocity is also slightly higher than the wall-normal component. For descending beads in Fig. 9b, the fluid shows a strong motion toward the wall and wall-normal velocity component of the fluid is significantly higher than its streamwise component. The small streamwise component is associated with a strong contribution of inward fluid motions (i.e., Q_3), which cancels out the streamwise component of the sweep motions. This is consistent with the observation in Fig. 7b where both Q_3 and Q_4 were significant around the descending beads. However, this is in contrast to previous investigations that associated only the descending beads with the sweep motions (Kiger and Pan 2002 and Vinkovic et al. 2011). The data also shows that about 45% of descending beads across the bottom half-channel are surrounded by the sweeps and 29% of descending beads are situated inside inward motions. The larger negative $\langle u_f \rangle_c$ in Fig. 9a agrees with Fig. 5a where the fluid surrounding ascending beads had a lower velocity than the ensemble fluid velocity. The small positive $\langle u_f \rangle_c$ in Fig. 9b also agrees with the slightly higher fluid velocity around descending beads relative to the ensemble fluid velocity. The positive $\langle v_f \rangle_c$ in Fig. 9a and negative $\langle v_f \rangle_c$ in Fig. 9b also agree with the $\langle V_f \rangle_c$ sign for ascending and descending beads in Fig 5b. The higher wall-normal fluid velocity around descending beads in Fig. 9b also supports the larger ρ_v of descending beads relative to the ascending ones in Fig. 6b.

The conditional average of fluid velocity fluctuation in the streamwise-spanwise plane is shown in Fig. 10 for the ascending and descending beads. Again, since the average spanwise velocity is zero, the absolute value of the spanwise velocity, $|w_f|$, is used. The figure shows a strong and uniform $\langle |w_f| \rangle_c$ around both ascending and descending beads. The magnitude of $\langle |w_f| \rangle_c$ is similar for both descending and ascending beads. Figure 10 shows that the ejection and sweep motions around the beads are accompanied by strong spanwise motions.

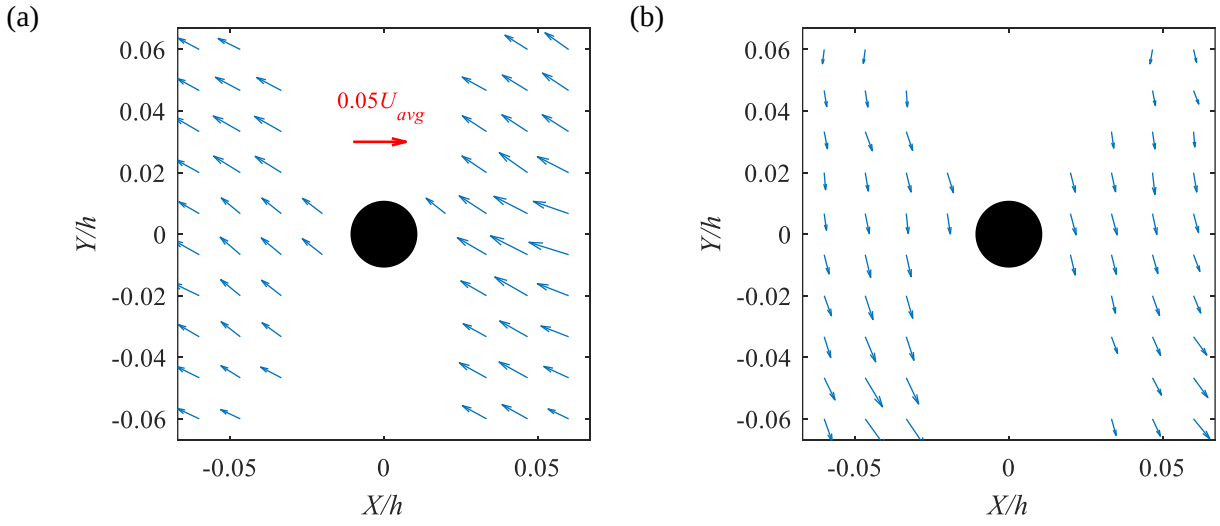

Fig. 9. Conditional average of fluid velocity fluctuation, $\langle u_f \rangle_c$ and $\langle v_f \rangle_c$, surrounding (a) ascending and (b) descending beads in the *XY* plane. The red arrow shows the reference vector size.

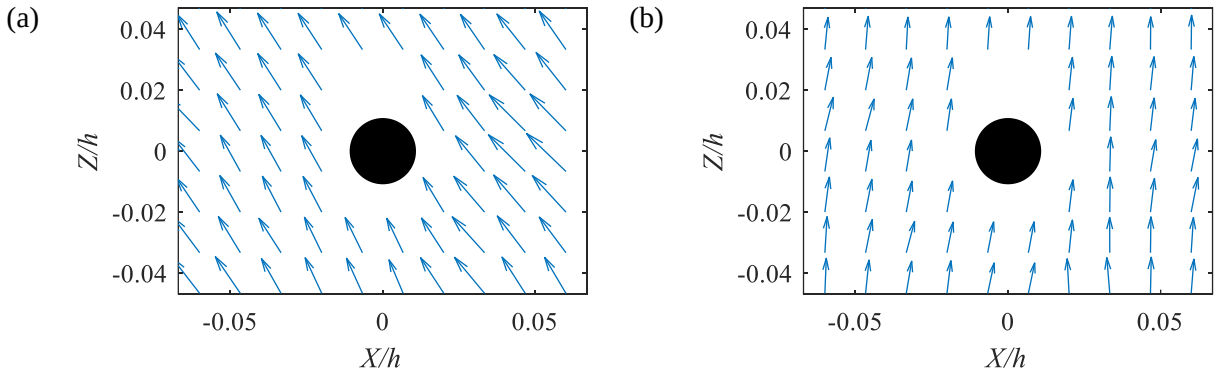

Fig. 10. Conditional average of fluid velocity fluctuation, $\langle u_f \rangle_c$ and $\langle |w_f| \rangle_c$, around (a) ascending and (b) descending beads in the *XZ* plane. The vectors are scaled relative to the reference vector shown in Fig. 9.

In Figs. 9 and 10, the fluid velocity fluctuations were calculated with respect to the ensemble average of the fluid velocity. However, to obtain the instantaneous fluid velocity relative to the bead velocity, the instantaneous tracer velocity must be conditionally averaged with respect to the enclosing bead velocity, i.e. $\boldsymbol{U}_r = \boldsymbol{U}_f - \boldsymbol{U}_b$. The result produced, for the *XY* plane, is shown in Fig. 11. For both ascending and descending beads, the relative streamwise velocity of the fluid is positive above the bead ($Y/h>0$) and negative below the bead ($Y/h<0$). This shear layer pattern stems from the positive wall-normal velocity gradient in the lower half of the channel.

In Fig. 11a, it can be seen that the surrounding fluid has a lower wall-normal velocity, i.e. negative $\langle V_r \rangle_c$, with respect to the ascending beads. In contrast, and shown in Fig. 11b, the fluid has a higher wall-normal velocity with respect to the descending beads, i.e. positive $\langle V_r \rangle_c$, which indicates that descending beads approach the wall faster than does the fluid. This may appear contradictory since the fluid is expected to carry the bead, and not slow it down. A possible explanation is that the wall-normal motion of a bead is initiated by a strong ejection or sweep. The fluid ejection/sweep velocity decays while the bead motion persists because of its longer response time. Therefore, based on conditional averaging, it appears that the beads lead the fluid in the wall-normal direction. A similar observation was made by Righetti and Romano (2004) for conditionally averaged Reynolds shear stress of ejection motions, i.e., $\langle uv \rangle_{Q2}$. They observed that $\langle uv \rangle_{Q2}$ of glass beads was larger than that of the fluid phase, which was also associated with the longer time-scale of the beads, allowing them to maintain their motion after they are lifted up by strong fluid ejections.

A clockwise vortex is observed in the conditional averages of Figs. 11a and 11b. The ascending beads are mostly located downstream of the vortex core, where $\langle V_r \rangle_c$ is negative, while the descending beads are at the upstream side of the vortex core where $\langle V_r \rangle_c$ is positive. It is also

interesting to note that the superposition of the velocity fields in Figs. 11a and 11b results in a simple shear flow showing the fluid velocity relative to both ascending and descending beads. The velocity gradient of the superposed flow field is $d\langle U_r\rangle/dY = 35\ s^{-1}$, which is smaller than $d\langle U_f\rangle/dY = 75\ s^{-1}$ of the ensemble fluid velocity at $y/h > 0.02$ ($y^+ > 20$). This smaller gradient shows that the beads are transported by low-shear fluid motions.

The relative velocity fields around ascending and descending beads in the *XZ* plane are shown in Fig. 12. The absolute value of the relative velocity is used for the spanwise direction, $\langle W_r\rangle_c = \langle|W_f - W_b|\rangle_c$. The figures show that $\langle|W_r|\rangle_c$ is uniform in the *XZ* plane and its value, approximately $0.03U_{avg}$, is similar for both ascending and descending beads. The spanwise slip here has an important effect on bead suspension since it can produce a lift force in the wall-normal direction that is similar to the lift caused by the streamwise slip.

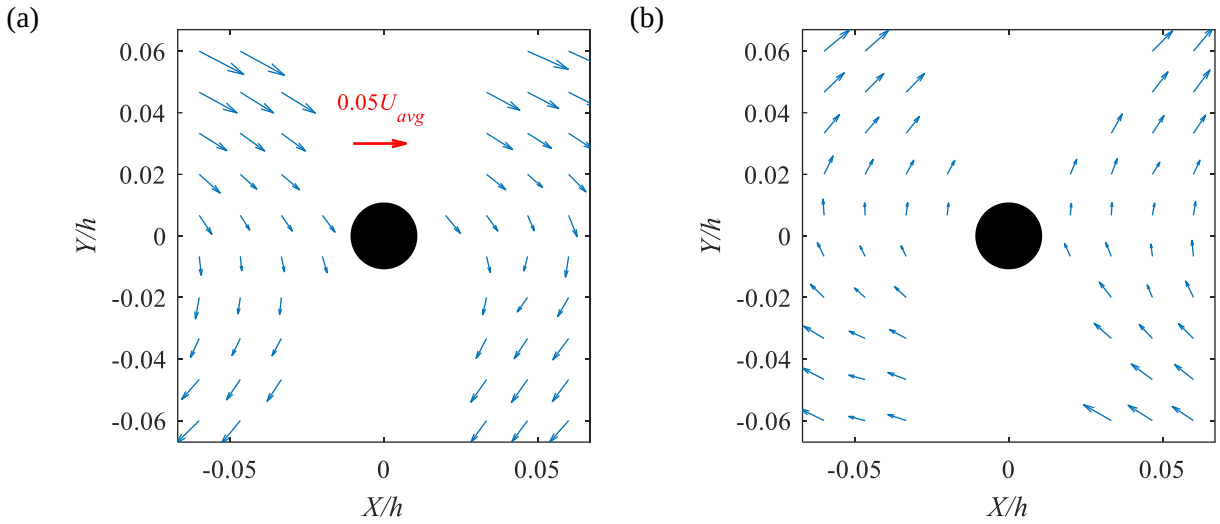

Fig. 11. Conditional average of fluid velocity relative to the beads, $\langle \boldsymbol{U}_r\rangle_c = \langle \boldsymbol{U}_f - \boldsymbol{U}_b\rangle_c$, in the *XY* plane for (a) ascending and (b) descending beads. The red arrow shows the reference vector size.

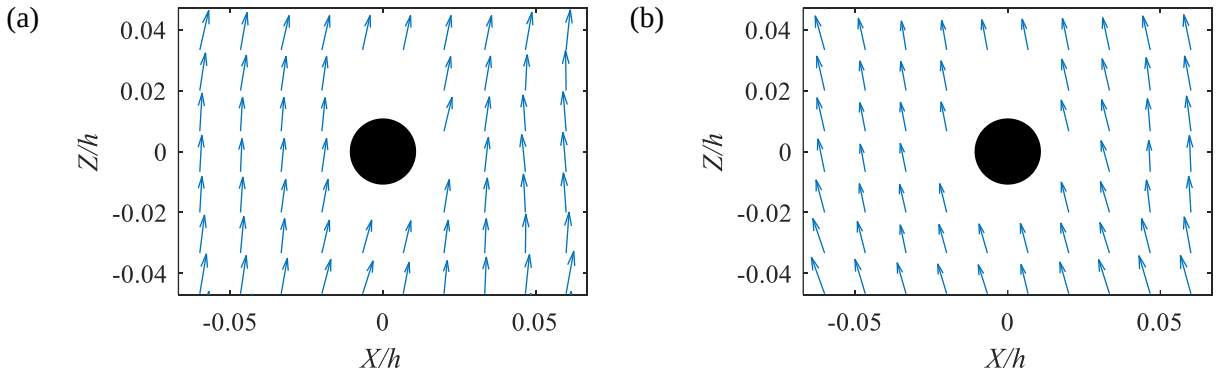

Fig. 12. Conditional average of fluid velocity in the *XZ* plane relative to the (a) ascending and (b) descending beads. For the spanwise component, the absolute value of relative velocity, i.e., $\langle|W_f - W_b|\rangle_c$, is used. The vectors are scaled similar to Fig. 11.

A slip velocity can be calculated by averaging the instantaneous relative velocity in the volume surrounding the beads. The average of slip velocity for all the beads in the bottom half-channel is $\langle|U_f - U_b|\rangle = 0.036U_{avg}$ in the *x* direction, $\langle|V_f - V_b|\rangle = 0.030U_{avg}$ in the *y* direction, and $\langle|W_f - W_b|\rangle = 0.033U_{avg}$ in the *z* direction, which corresponds to particle Reynolds numbers, Re_p, of 17.8, 14.7, and 16.3 in the *x*, *y*, and *z* directions, respectively. If conditional averaging is carried out at specific *y/h* locations, a larger Re_p of 33.5 is observed at $y/h = 0.06$ that gradually reduces to 11.8 at $y/h = 0.46$. The Re_p calculated based on apparent slip velocity, $\langle U_f\rangle - \langle U_b\rangle$, across the bottom half-channel is 6.0 in streamwise, 1.7 in wall-normal, and 2.1 in spanwise directions. Therefore, use of the apparent slip velocity to calculate Re_p produces a value that is lower by a factor of one half to one third. This is an important result since the Re_p is a key parameter in determining turbulence modulation in particle-laden flows.

5. Accelerating/decelerating beads

Acceleration or deceleration of a bead indicates momentum exchange with the fluid phase through different forces. For finite-size particles, these forces include ~~Stokes~~ drag force, added mass, and Basset history force. In this section, the flow pattern surrounding the beads is conditionally averaged based on whether a bead is subject to acceleration or deceleration in the streamwise direction. The conditional averages show the pattern of relative fluid velocity around the bead, and therefore, indicate the direction of ~~Stokes~~ the drag force. Such an analysis can be helpful for numerical simulations since in most cases only ~~Stokes~~ the drag force is considered. We define a_b as the instantaneous streamwise acceleration of a bead, which is obtained from the Lagrangian trajectories obtained using 4D-PTV.

5.1. Conditionally averaged velocity

The streamwise, wall-normal, and spanwise bead velocity and the surrounding fluid velocity are conditionally averaged based on the sign of the a_b and are shown in Fig. 13. The mean fluid velocity (ensemble average) is also shown in Fig. 13a for comparison. In Fig. 13a, $\langle U_b\rangle_c$ of accelerating beads is lower than the surrounding fluid velocity. Hence, on average, there is a positive slip velocity, which generates a force to accelerate the beads. The streamwise slip velocity slightly increases with decreasing distance from the wall. In Fig. 13b, the accelerating beads are shown to have a positive $\langle V_b\rangle_c$, which indicates that they ascend toward the centre of the channel as they accelerate.

The decelerating beads at $y/h > 0.25$ ($y^+ > 250$) of Fig. 13a have a slightly higher velocity than the surrounding fluid. The beads also have a negative $\langle V\rangle_c$ in Fig. 13b, which shows that they move towards the wall and into the lower-velocity layers, and the resulting drag force decelerates the beads. However, at $y/h < 0.25$, decelerating beads are slower than the surrounding fluid, i.e. $\langle U_b\rangle_c$-

$\langle U_f \rangle_c < 0$, while they still have a negative $\langle V \rangle_c$. In order to further evaluate this observation, the average of instantaneous slip, $\langle U_f - U_b \rangle$ was also calculated. It was found to be positive and equal to $0.01U_{avg}$. A positive slip velocity means that deceleration of the beads is not associated with the drag force. Therefore, at $y/h < 0.25$, other forces such as added mass, Basset force, or friction due to collision and momentum exchange with the wall contribute to bead deceleration.

Values of $\langle |W| \rangle_c$ for accelerating and decelerating beads, and the surrounding fluid, are shown in Fig. 13c. The beads have a higher spanwise velocity than the surrounding fluid, which is similar to the trend in the wall-normal direction. Again, as was the case for the wall-normal motions, it is hypothesized that the beads preserve their spanwise velocity for a greater duration than the fluid phase, which results in a higher average bead velocity. The spanwise velocity profiles are almost identical to the velocity profiles shown for ascending and descending beads in Fig. 5c; the effect of sampling criterion on spanwise velocities is negligible.

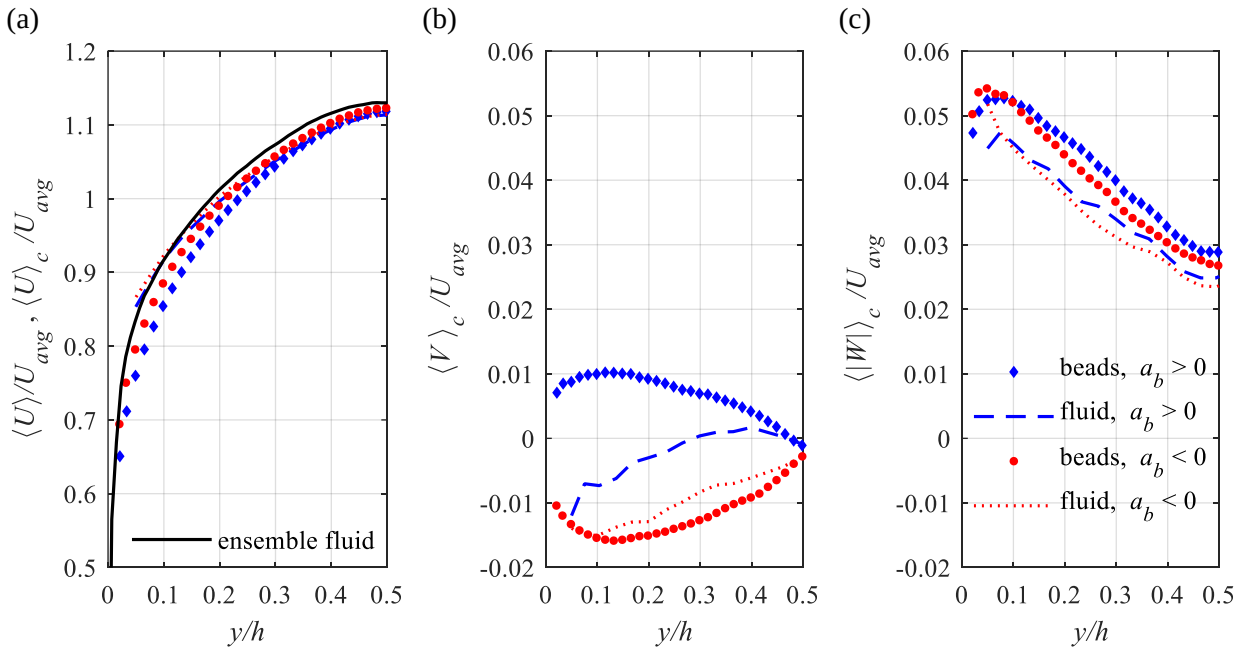

Fig. 13. Conditionally average of (a) streamwise, (b) wall-normal, and (c) absolute spanwise velocity of the beads and their surrounding fluid sampled based on a_b sign.

5.2. Velocity fields around the beads

To relate the 3D flow field with the bead dynamics, the relative velocity fields, $\langle \boldsymbol{U}_r \rangle_c = \langle \boldsymbol{U}_f - \boldsymbol{U}_b \rangle_c$, around accelerating ($a_b > 0$) and decelerating beads ($a_b < 0$) are illustrated in Fig. 14 for the *XY* plane and in Fig. 15 for the *XZ* plane. The conditional averaging is carried out across the bottom half-channel. It was shown in Fig. 13a that accelerating beads are slower than their surrounding fluid across the bottom half-channel and, as a result, the drag force contributes to their streamwise acceleration. However, the relative velocity is not uniform around the bead. In Figure 14a, a net positive streamwise $\langle U_r \rangle_c$ is seen above the bead at $Y > 0$ and a negative relative velocity is present

below the bead at $Y < 0$. The relative velocity field is uniform and has a positive value in the whole XZ plane, as shown in Fig. 15a. Comparing Figs. 11 and 14, we see that the relative velocity fields around accelerating and decelerating beads have a structure that is similar to the flow pattern around ascending and descending beads in the XY plane, but with a lower wall-normal velocity. The velocity field around decelerating beads, shown in Fig. 14b has a positive relative velocity at $Y > 0$ and a negative relative velocity at $Y < 0$. The averaged relative velocity in this plane is negative. Despite the presence of accelerating beads, no uniform trend is observed in the XZ plane of Fig. 15b.

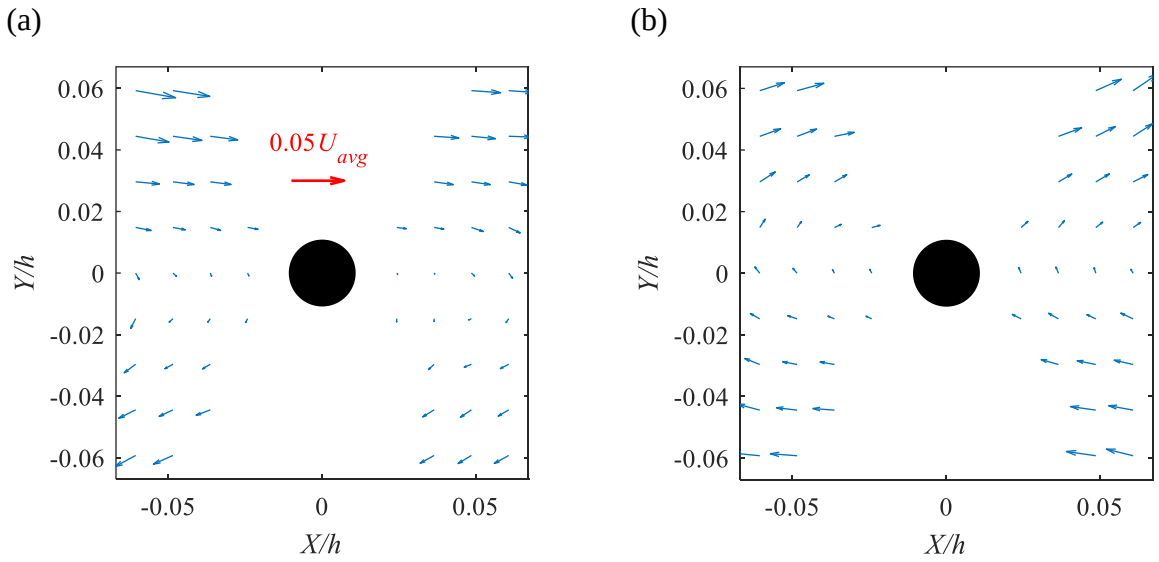

Fig. 14. Conditional average of relative fluid velocity, $\langle \boldsymbol{U}_r \rangle_c = \langle \boldsymbol{U}_f - \boldsymbol{U}_b \rangle_c$ in the XY plane surrounding (a) accelerating ($a_b > 0$) and (b) decelerating beads ($a_b < 0$). The red arrow shows the reference vector size.

(a) (b)

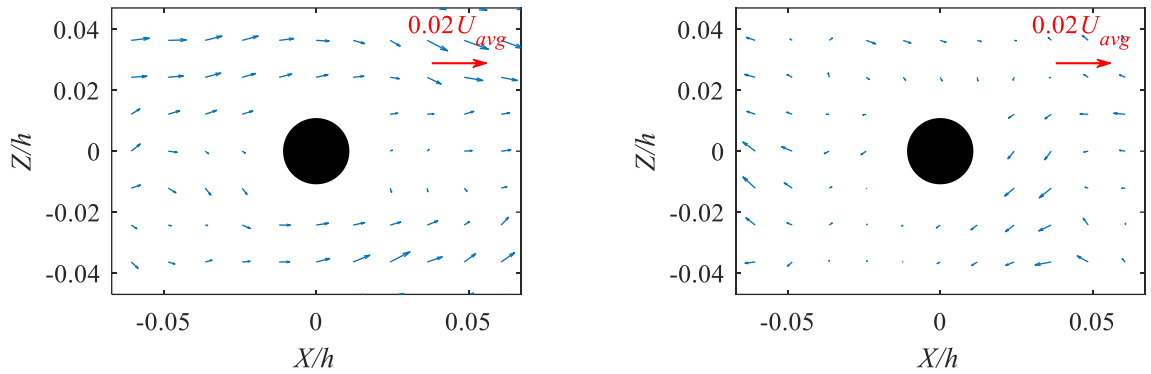

Fig. 15. Conditional average of relative velocity field, $\langle \boldsymbol{U}_r \rangle_c = \langle \boldsymbol{U}_f - \boldsymbol{U}_b \rangle_c$ in the *XZ* plane surrounding (a) accelerating beads ($a_b > 0$), and (b) decelerating beads ($a_b < 0$). The red arrow shows the reference vector size.

6. Bead pathlines

The previous sections showed that bead motion is accompanied by a significant spanwise velocity component, which is higher closer to the wall. In order to understand the phenomenon that produces this spanwise motion, bead pathlines are examined here. Fig. 16 shows four sample pathlines and their projection on the *xy*, *yz*, and *xz* planes, within the field of view of 4D-PTV. The selected pathlines are representative of different pathline patterns observed by visual inspection, and they are numbered in the *yz* plane of Fig. 16. Pathlines (1) and (2) do not show frequent change in their wall-normal and spanwise motions; pathline (1) is inclined 4° toward the wall, and pathline (2) has an angle of 5° away from the wall. These pathlines are usually located in the outer layer, closer to the channel centre. Pathlines (3) and (4), on the other hand, show frequent changes in the direction of their wall-normal and spanwise motions, which result in a spiral motion around the *x* axis. The beads shown by pathlines (3) and (4) move forward by a distance of $\Delta x/h \sim 3.5$ as they undergo two full spins around a streamwise axis.

The frequent change in the bead wall-normal motion was also observed in the experimental studies of Sumer and Oguz (1978) and Rashidi et al. (1990) but the bead spanwise motion was not revealed by their 2D measurements. Pathlines (3) and (4) spiral in the *yz* plane and result in the observed spanwise bead velocity. The spiral motion of the beads and the change in their direction of motion is more apparent closer to the wall since the flow time-scale is smaller and the spiral motions are captured within the measurement domain. Pathlines (1) and (2) are associated with motions having a longer time scale since they are farther away from the wall. It should also be noted that the axes in Fig. 16 do not have the same scale, and the displacements are magnified in the *y* and *z* directions.

Inspection of the detected pathlines shows that the majority of descending beads approach the wall and change direction when they reach $y/h \sim 0.05$ ($y^+=50$). To characterize this direction change statistically, the local maxima (y_{max}) and minima (y_{min}) in the *y* position are detected using the slope (dy/dt) of the trajectories. An example of such a point is indicated by points A and B in Fig. 16. The same analysis is also conducted to detect the points where the spanwise motion of the beads

changes direction; that is, extrema in the z direction indicated at z_{ext}, like point C in Fig. 16. The probability density function (pdf) of the number of detected y_{mix}, y_{max}, and z_{ext} is presented in Fig. 17a. It is observed that the pdf of y_{min} is larger close to the wall, confirming that most of the descending paths change direction in this region. In contrast, the pdf of y_{max} increases with distance from the wall; that is, with increasing distance from the wall, a greater number of ascending motions change direction and approach the wall. The change in the direction of motion from descending to ascending is hypothesized to result from ejection motions of the fluid, or collision of the beads with the wall. Because the ejections are stronger near the wall, the changes in the descending motions occur more frequently in this region. On the other hand, the upward moving beads usually change direction because of gravitational and drag forces, as highlighted in Fig. 11a. This results in the gradual pdf increase for y_{max} with an increase of y. Figure 17a also shows that the number of spanwise extrema reduces with decreasing y, which is associated with stronger spiral motions in the near-wall region.

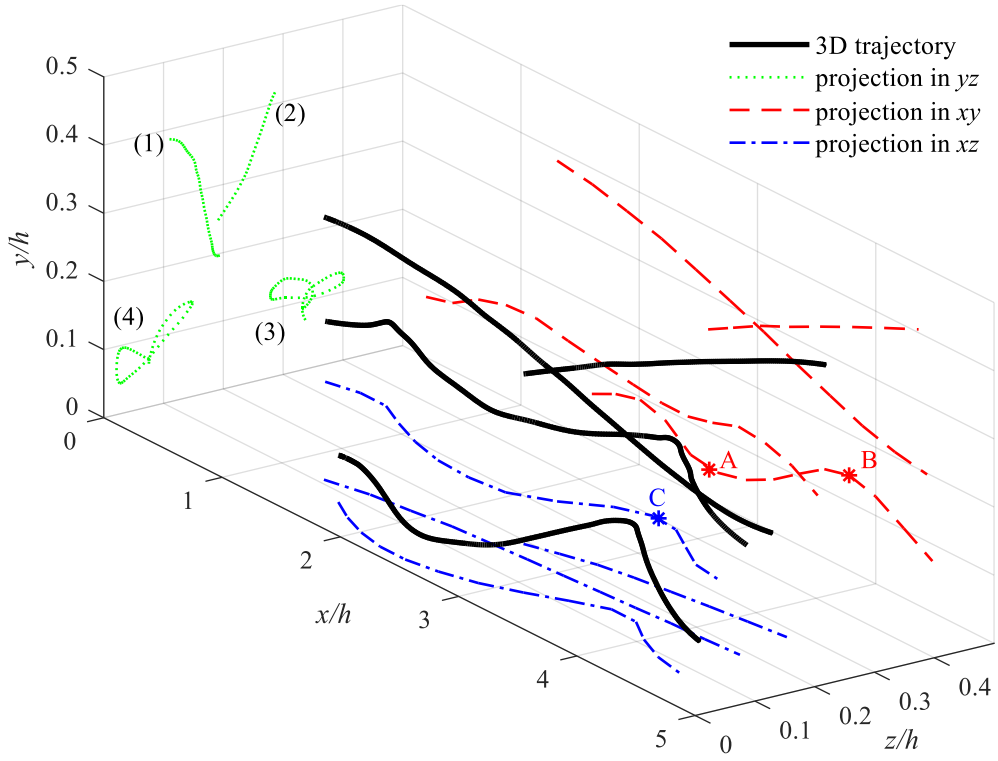

Fig. 16. Sample 3D trajectories of beads (shown in black) and their projection on *xy*, *yz*, and *xz* planes. The spiral of the pathlines (3) and (4) about *x* direction can be recognized as they move forward. For better representation, *y* and *z* axes are magnified by a factor of 3.5 with respect to *x* axis.

In order to identify the effect of particle concentration and potential particle-particle collisions, the number density profile of the beads is shown in Fig. 17b. In this figure, the number of beads in each bin (Δy_{bin} = 0.4 mm) is normalized by the average number of beads per bin (N_{avg}). It can be seen that the distribution is almost uniform; the maximum number density is only 17% larger than the minimum number density (N_{max}/N_{min} = 1.17). Hence, variation in the number density of

particles is small and is not expected to be associated with an increased probability of particle-particle collisions.

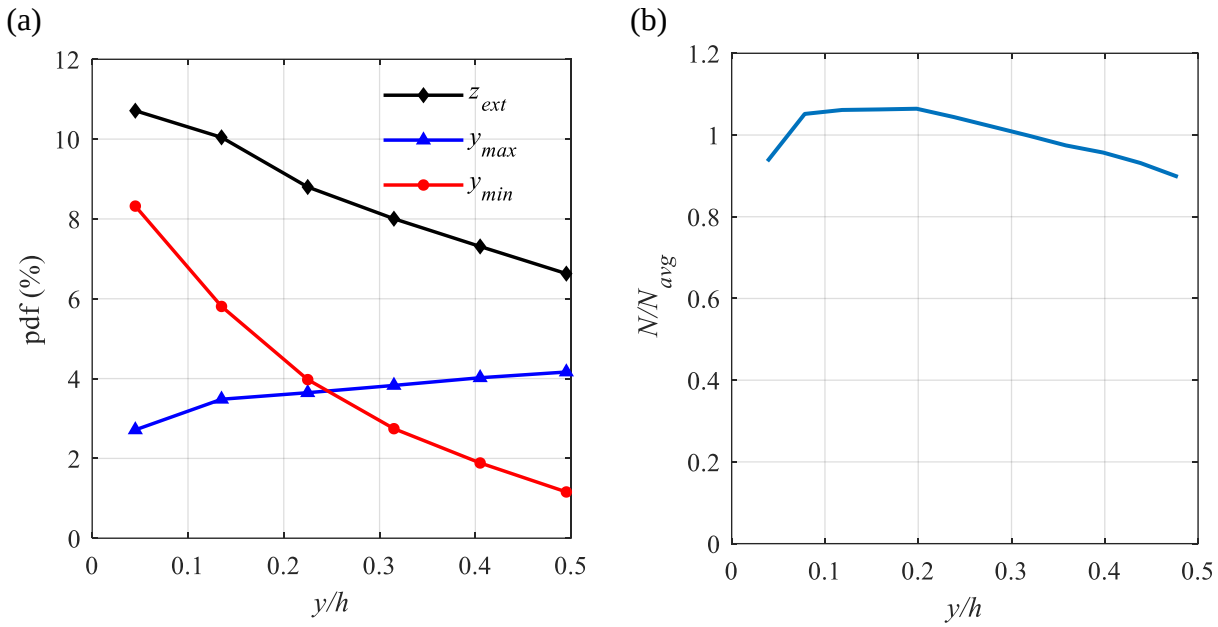

Fig. 17. (a) The pdf of the number of local maximums (y_{max}) and minimums (y_{min}) in the wall-normal position of the beads, and the number of local extremums in the spanwise position of the beads (z_{ext}). (b) Normalized number density profile of the beads across the bottom-half channel.

7. Conclusion

The interaction between the beads and the fluid phase was investigated in a particle-laden turbulent channel flow at *Re* = 20,000. The particulate phase consisted of nearly neutrally buoyant beads with an average diameter of 370 μm and *St* of 2.7 at a volumetric concentration of 0.1%. Three-dimensional time-resolved particle tracking velocimetry (4D-PTV), based on the shake-the-box method, was used to measure the instantaneous velocity of the beads and the fluid phase

simultaneously. The beads' velocity and the surrounding flow were conditionally sampled based on the wall-normal velocity (ascending versus descending beads) and the streamwise acceleration of the beads (accelerating versus decelerating beads).

The conditional averaging, based on the wall-normal velocity, showed that the streamwise velocity of the ascending beads and the surrounding fluid is lower than the ensemble fluid velocity. This velocity deficit is associated with the preferential accumulation of the ascending beads in the low-speed regions. In contrast, the descending beads and their nearby fluid had nearly the same average velocity as the ensemble fluid velocity. The apparent slip velocity, based on the difference of the average bead and flow velocity, was higher for the ascending beads. It was also observed that the spanwise bead velocity was higher than the wall-normal bead velocity. At $y/h < 0.25$ ($y^+ < 250$), the streamwise velocity of descending beads showed a strong correlation with the nearby fluid. However, this correlation decreased with increasing wall-normal distance since the preferential accumulation of descending beads in sweep motions decreased. The descending beads also had a stronger correlation with the wall-normal flow velocity. For the ascending beads, with increasing wall-normal distance, both their correlation with surrounding flow and the extent of accumulation in ejection motions increased.

The conditional sampling based on bead acceleration showed that accelerating beads move away from the wall and have a lower velocity than the surrounding flow. Away from the wall, at $y/h > 0.25$, the decelerating beads also have a higher streamwise velocity than the surrounding fluid. Therefore, for both cases, the drag force caused by slip velocity contributes to their acceleration/deceleration. However, at $y/h < 0$, decelerating beads have a lower velocity than the surrounding flow, suggesting that the ~~Stokes~~ drag force is not sufficient to model the dynamics of nearly buoyant beads.

The simultaneous measurements of bead and carrier phase velocities showed that the slip velocity calculated from the difference between the average bead and fluid velocities, $\langle U_f \rangle_c$-$\langle U_b \rangle_c$, significantly underestimates the actual instantaneous slip velocity. The conditionally averaged flow fields also showed a remarkable spanwise slip velocity. The flow velocity pattern with respect to an enclosed bead appeared as a clockwise vortex in the *XY* plane, with a significant wall-normal velocity gradient. The conditionally averaged wall-normal velocity of the fluid appeared to oppose the motion of ascending and descending beads. This observation supported the notion that the motion of a bead begins with fluid ejection that quickly decays, while the bead sustains its motion for a longer time.

The beads' pathlines showed successive upward and downward motions, and also successive changes in the direction of spanwise motion. The latter resulted in a spiral motion around the *x* direction with a shorter turn-over time in the near-wall region ($y/h < 0.25$). The descending beads frequently changed direction in the near-wall region when approaching the wall, while ascending beads frequently changed direction farther away from the wall.

Appendix A: Uncertainty analysis

The random error in the velocity statistics for the beads and the fluid phase are evaluated here based on the statistical convergence of the data at y^+ = 30, 250, and 500 (corresponds to y/h = 0.03, 0.23, and 0.46). Figure 18 shows the statistical convergence of the velocity statistics of the beads at y^+ = 500. The horizontal axis of the figure shows the number of data points used for averaging (n) normalized by the total number of data in the bin (N). The random error is estimated as the difference between the maximum and minimum of the averaged quantity using the last 20% of data points. The results are presented in Table 2 for the beads and in Table 3 for the fluid phase.

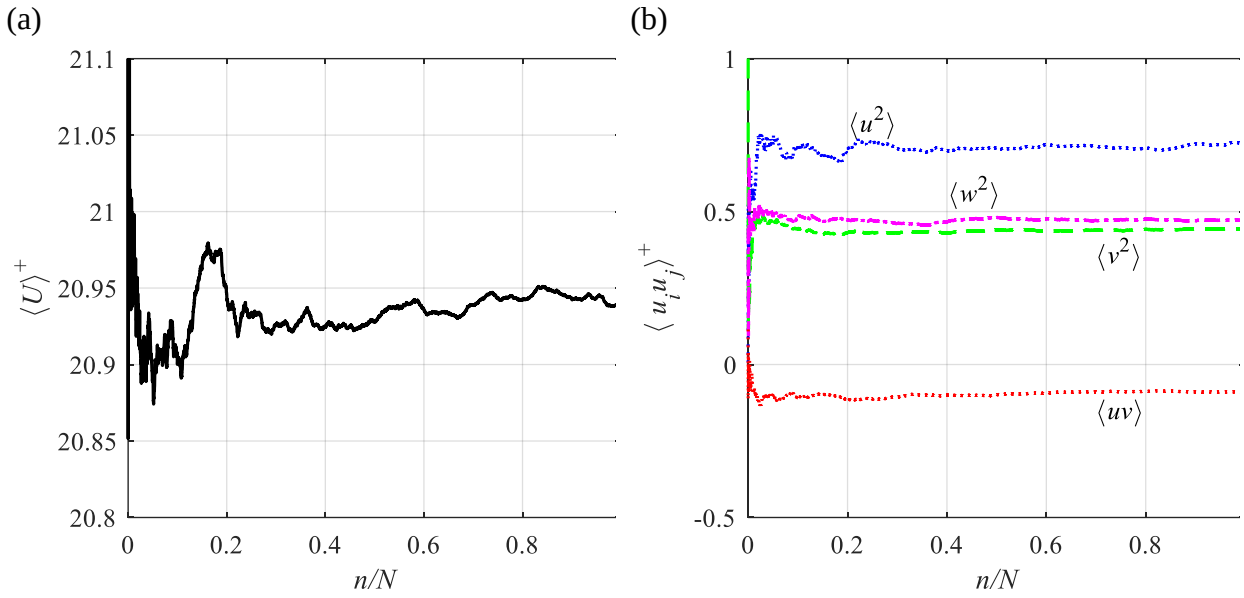

Fig. 18 Statistical convergence of (a) the mean velocity and (b) Reynold stresses of the beads at y^+ = 500 (y/h = 0.46). The maximum and minimum values for n/N of 0.8 to 1 are used to estimate the random error.

Table 2 Estimated random error for beads' statistics.

Parameter	y^+ = 30	y^+ = 250	y^+ = 500
$\langle U_b \rangle^+$	0.025	0.011	0.013
$\langle u_b^2 \rangle^+$	0.030	0.040	0.020
$\langle v_b^2 \rangle^+$	0.006	0.006	0.003
$\langle w_b^2 \rangle^+$	0.011	0.010	0.006
$\langle u_b v_b \rangle^+$	0.010	0.006	0.004

Table 3 Estimated random error for velocity statistics of the fluid phase.

Parameter	$y^+ = 30$	$y^+ = 250$	$y^+ = 500$
$\langle U_f \rangle^+$	0.021	0.012	0.007
$\langle {u_f}^2 \rangle^+$	0.090	0.020	0.009
$\langle {v_f}^2 \rangle^+$	0.020	0.003	0.004
$\langle {w_f}^2 \rangle^+$	0.030	0.006	0.004
$\langle u_f v_f \rangle^+$	0.020	0.005	0.007

References

Atherton TJ, Kerbyson DJ (1999) Size invariant circle detection. Image Vis Comput 17:795–803. doi: 10.1016/S0262-8856(98)00160-7

Bellani G, Byron ML, Collignon AG, et al (2012) Shape effects on turbulent modulation by large nearly neutrally buoyant particles. J Fluid Mech 712:41–60. doi: 10.1017/jfm.2012.393

Brooke JW, Kontomaris K, Hanratty TJ, McLaughlin JB (1992) Turbulent deposition and trapping of aerosols at a wall. Phys Fluids A Fluid Dyn 4:825–834. doi: 10.1063/1.858299

Clauser FH (1956) The Turbulent Boundary Layer. Adv Appl Mech 4:1–51. doi: 10.1016/S0065-2156(08)70370-3

Elghobashi S (1991) Particle-laden turbulent flows: direct simulation and closure models. Appl Sci Res 48:301–314. doi: 10.1007/BF02008202

Ghaemi S, Scarano F (2010) Multi-pass light amplification for tomographic particle image velocimetry applications. Meas Sci Technol 21:127002.

Ji C, Munjiza A, Avital E, et al (2013) Direct numerical simulation of sediment entrainment in turbulent channel flow. Phys Fluids 25:56601. doi: 10.1063/1.4807075

Kaftori D, Hetsroni G, Banerjee S (1995) Particle behavior in the turbulent boundary layer. I. Motion, deposition, and entrainment. Phys Fluids 7:1095–1106. doi: 10.1063/1.868551

Kiger KT, Pan C (2002) Suspension and turbulence modification effects of solid particulates on a horizontal turbulent channel flow. J Turbul 3:N19. doi: 10.1088/1468-5248/3/1/019

Kiger KT, Pan C (2000) PIV technique for the simultaneous measurement of dilute two-phase flows. Trans Soc Mech Eng J FLUIDS Eng 122:811–818.

Lee M, Moser RD (2015) Direct numerical simulation of turbulent channel flow up to Reτ~ 5200. J Fluid Mech 774:395–415. doi: DOI: 10.1017/jfm.2015.268

Lelouvetel J, Bigillon F, Doppler D, et al (2009) Experimental investigation of ejections and sweeps involved in particle suspension. Water Resour Res 45:n/a--n/a. doi: 10.1029/2007WR006520

Li D, Wei A, Kun L, Jianren F (2016) Direct numerical simulation of a particle-laden flow in a flat plate boundary layer. Int J Multiph Flow 79:124–143. doi: 10.1016/J.IJMULTIPHASEFLOW.2015.10.011

Marchioli C, Soldati A (2002) Mechanisms for particle transfer and segregation in a turbulent boundary layer. J Fluid Mech 468:283–315. doi: DOI: 10.1017/S0022112002001738

Marchioli C, Soldati A, Kuerten JGM, et al (2008) Statistics of particle dispersion in direct numerical simulations of wall-bounded turbulence: Results of an international collaborative benchmark test. Int J Multiph Flow 34:879–893. doi: 10.1016/J.IJMULTIPHASEFLOW.2008.01.009

Milojević D (1990) Lagrangian Stochastic-Deterministic (LSD) Predictions of Particle Dispersion in Turbulence. Part Part Syst Charact 7:181–190. doi: 10.1002/ppsc.19900070132

Nino Y, Garcia MH (1996) Experiments on particle-turbulence interactions in the near-wall region of an open channel flow: implications for sediment transport. J Fluid Mech 326:285. doi: 10.1017/S0022112096008324

Oliveira JLG, van der Geld CWM, Kuerten JGM (2015) Lagrangian velocity and acceleration statistics of fluid and inertial particles measured in pipe flow with 3D particle tracking velocimetry. Int J Multiph Flow 73:97–107. doi: 10.1016/J.IJMULTIPHASEFLOW.2015.03.017

Oliveira JLG, van der Geld CWM, Kuerten JGM (2013) Lagrangian and Eulerian Statistics of Pipe Flows Measured with 3D-PTV at Moderate and High Reynolds Numbers. Flow, Turbul Combust 91:105–137. doi: 10.1007/s10494-013-9457-9

Rashidi M, Hetsroni G, Banerjee S (1990) Particle-turbulence interaction in a boundary layer. Int J Multiph Flow 16:935–949. doi: 10.1016/0301-9322(90)90099-5

Righetti M, Romano GP (2004) Particle–fluid interactions in a plane near-wall turbulent flow. J Fluid Mech 505:93–121. doi: DOI: 10.1017/S0022112004008304

Scarano F, Poelma C (2009) Three-dimensional vorticity patterns of cylinder wakes. Exp Fluids 47:69. doi: 10.1007/s00348-009-0629-2

Schanz D, Gesemann S, Schröder A (2016) Shake-The-Box: Lagrangian particle tracking at high particle image densities. Exp Fluids 57:70. doi: 10.1007/s00348-016-2157-1

Schlichting H, Gersten K (2017) Boundary-Layer Theory. Springer, Berlin, Heidelberg

Shao X, Wu T, Yu Z (2012) Fully resolved numerical simulation of particle-laden turbulent flow in a horizontal channel at a low Reynolds number. J Fluid Mech 693:319–344. doi: 10.1017/jfm.2011.533

Soloff SM, Adrian RJ, Liu Z-C (1997) Distortion compensation for generalized stereoscopic particle image velocimetry. Meas Sci Technol 8:1441.

Sumer BM (1974) Mean velocity and longitudinal dispersion of heavy particles in turbulent open-channel flow. J Fluid Mech 65:11. doi: 10.1017/S0022112074001212

Sumer BM, Oguz B (1978) Particle motions near the bottom in turbulent flow in an open channel. J Fluid

Mech. doi: 10.1017/S0022112078001020

Sutherland AJ (1967) Proposed mechanism for sediment entrainment by turbulent flows. J Geophys Res 72:6183–6194. doi: 10.1029/JZ072i024p06183

Suzuki Y, Ikenoya M, Kasagi N (2000) Simultaneous measurement of fluid and dispersed phases in a particle-laden turbulent channel flow with the aid of 3-D PTV. Exp Fluids 29:S185--S193. doi: 10.1007/s003480070020

Tennekes H, Lumley JL (1972) A First Course in Turbulence. MIT Press

van Hout R (2011) Time-resolved PIV measurements of the interaction of polystyrene beads with near-wall-coherent structures in a turbulent channel flow. Int J Multiph Flow 37:346–357. doi: 10.1016/J.IJMULTIPHASEFLOW.2010.11.004

van Hout R (2013) Spatially and temporally resolved measurements of bead resuspension and saltation in a turbulent water channel flow. J Fluid Mech 715:389–423. doi: 10.1017/jfm.2012.525

Vinkovic I, Doppler D, Lelouvetel J, Buffat M (2011) Direct numerical simulation of particle interaction with ejections in turbulent channel flows. Int J Multiph Flow 37:187–197. doi: 10.1016/j.ijmultiphaseflow.2010.09.008

Wieneke B (2005) Stereo-PIV using self-calibration on particle images. Exp Fluids 39:267–280. doi: 10.1007/s00348-005-0962-z

Wieneke B (2008) Volume self-calibration for 3D particle image velocimetry. Exp Fluids 45:549–556. doi: 10.1007/s00348-008-0521-5

Wieneke B (2013) Iterative reconstruction of volumetric particle distribution. Meas Sci Technol 24:24008.

Willmarth WW, Lu SS (1972) Structure of the Reynolds stress near the wall. J Fluid Mech 55:65. doi: 10.1017/S002211207200165X

Yung BPK, Merry H, Bott TR (1989) The role of turbulent bursts in particle re-entrainment in aqueous systems. Chem Eng Sci 44:873–882. doi: 10.1016/0009-2509(89)85260-1

Zamansky R, Vinkovic I, Gorokhovski M (2011) Acceleration statistics of solid particles in turbulent channel flow. Phys Fluids 23:113304. doi: 10.1063/1.3662006